Title

Impact of Nano- and Mesoscales on Macroscopic Cation Conductivity in Perfluorinated-Sulfonic-Acid Membranes

Journal

The Journal of Physical Chemistry C, 121(51)

ISSN

1932-7447

Authors

Crothers, Andrew R
Radke, Clayton J
Weber, Adam Z

Publication Date

2017-12-28

DOI

10.1021/acs.jpcc.7b07360

Impact of Nano- and Mesoscales on Macroscopic Cation Conductivity in Perfluorinated-Sulfonic-Acid Membranes

Andrew R. Crothers,[†,‡] Clayton J. Radke[†,§] and Adam Z. Weber[‡,]*

[†]Chemical and Biomolecular Engineering Department, University of California, Berkeley, California 94720, USA

[‡]Energy Conversion Group, Energy Technologies Area, [§]Earth Sciences Division Lawrence Berkeley National Laboratory, Berkeley, CA 94720, USA

**Corresponding author, email: azweber@lbl.gov, Phone: (510) 486-6308, Fax: (510) 486-7303*

ABSTRACT

A mean-field local-density theory is outlined for ion transport in perfluorinated-sulfonic-acid (PFSA) membranes. A theory of molecular-level interactions predict nanodomain and macroscale conductivity. The effects of solvation, dielectric saturation, dispersion forces, image charge, finite size, and confinement are included in a physically consistent 3D-model domain geometry. Probability-distribution profiles of aqueous cation concentration at the domain-scale are in agreement with atomistic simulations using no explicit fitting parameters. Measured conductivities of lithium-, sodium-, and proton-form membranes with equivalent weights of 1100, 1000, and 825 g/mol(SO3) validate the macroscale predictions using a single-value mesoscopic fitting parameter. Cation electrostatic interactions with pendant sulfonate groups are the largest source of migration resistance at the domain-scale. Tortuosity of ionically conductive domains is the largest source of migration resistance at the macroscale. Our proposed transport model is consistent across multiple lengthscales. We provide a compelling methodology to guide material design and optimize performance in energy-conversion applications of PFSA membranes.

Introduction

Ion transport in cation-exchange membranes is fundamentally linked to the performance of a variety of burgeoning clean-energy technologies such as polymer-electrolyte fuel cells (PEFC).[1] A prototypical PEFC membrane consists of a phase-separated polymer with interconnected conductive, nanoscale, aqueous domains embedded in a nonconductive matrix that provides structural integrity and durability.[2-4] Interactions between appended charged polymer groups and aqueous counterions cause ion-transport behavior in the aqueous domains to differ from that in bulk aqueous solution.[3-4] To understand how molecular interactions among polymer, water, and ions at the nanoscale mediate transport at the macroscale, we formulate a multiscale mechanistic model for ion transport in fuel-cell membranes.

Perfluorinated-sulfonic-acid (PFSA) copolymers are the prototypical PEFC membrane material. PFSAs consist of a fluorocarbon backbone with perfluoroether sidechains that terminate in negatively charged sulfonate groups.[2] The sulfonate anion is charge compensated by an aqueous cation, such as a proton. Unfavorable interactions between the hydrophilic sulfonate moiety and the hydrophobic backbone cause the polymer to phase separate into solid polymer bundles and an interconnected network of ionically conductive, hydrophilic domains or "pores."[2-5]

Because the ionic conductivity of PFSA membranes increases drastically with water content, PEFC membranes typically operate under humidified conditions.[1] A wet environment leads to water absorption into the hydrophilic domains of the membrane with the subsequent water content described as the molar ratio of water per sulfonate site, λ (mole H_2O/mole SO_3^-).[4] Because the sulfonate anions are immobilized by covalent bonds to the polymer matrix, electrolyte conduction through the membrane is accomplished by movement of aqueous cations.[3]

The amount of absorbed water controls the degree to which the cation and the sulfonate group dissociate.[3, 6] Figure 1a depicts a completely dry PFSA domain in which the sulfonate group and cation form an ionically bound ion pair.[3, 6-7] The proton exists as a hydronium cation since desorption of the

constituent water molecule occurs only at extreme temperatures (>200 °C).[4] Figure 1b depicts water solvating the bound ions. At low water contents, there is not enough water to separate the ions; they remain as bound contact pairs.[3, 6-7] Ions forming salt complexes or contact pairs are immobile and do not facilitate conduction.[7] Figure 1c depicts water completely solvating the ions at higher water contents allowing complete ion dissociation.[3, 6-7]

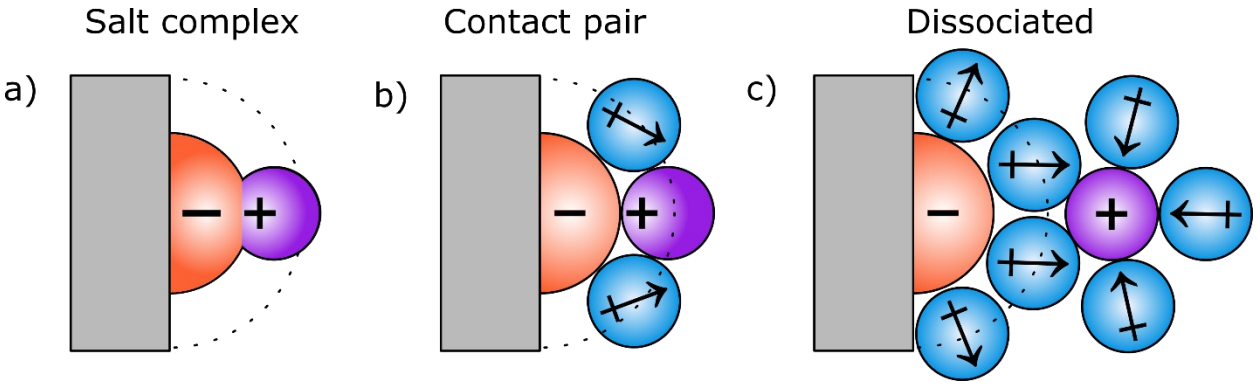

Figure 1. Depiction of the cation center of charge (+) and water dipole (↠) distributions around a pendant sulfonate group (–). Solid lines denote the hard-sphere radius. Dotted lines denote the first solvation shell of the sulfonate group. Grey region denote PFSA polymer. a) In completely dry conditions, the sulfonate ions and cations are tightly bound as salt complex. b) In low-water conditions, ions form contact pairs. c) In high-water conditions some of the ion pairs dissociate.

Water content increases conductivity because hydration dissociates ion pairs,[3, 8-15] increases the hydrophilic volume fraction of the polymer, [16-18] and decreases the tortuosity between domains. [13, 18-22] Conversely, increasing water content otherwise decreases conductivity because the concentration of free aqueous cations is lower.[17-18, 23] Quantifying the relative contributions of these factors is challenging because they are all coupled to water content.[3, 17, 24] Research observations are often attributed to any one of these factors without considering the others.[3, 18, 24] The modeling approach herein elucidates these factors and their specific effects on measurable macroscale properties.

Molecular-dynamics (MD) and *ab-initio* simulations provide invaluable understanding of intermolecular interactions among polymer, solvent, and ions in the nanodomains, but often do not describe transport processes.[9-10, 12, 25-31] Conversely, microcontinuum models provide crucial insights into transport processes in the nanodomains, but current models have selective applicability to PEFC systems

because they do not examine varying hydration[32-33] or exclude relevant nanoscale interactions, such as solvation energies.[8, 23, 34-37] Both approaches often focus on nanoscale properties without connection to macroscopic observables.[4] Our model is grounded in physical descriptions provided by microcontinuum theories and atomistic simulations but goes beyond previous work by giving a consistent mechanistic description within the nanodomains and at the mesoscale as a function of hydration.

To elucidate how molecular-level interactions among solvent, ions, and polymer matrix affect macroscopic properties, a quantitative model is developed for domain-scale physics of cation conduction in PFSA membranes. The approach includes molecular-scale interactions including finite-size, confinement, ion solvation, dielectric saturation, image charge, and dispersion forces. The proposed micro/macro-scale model is validated against both atomistic simulations[26, 29] and experimentally measured ion conductivity.[38] To ensure physical veracity, realistic geometric parameters are adopted from direct imaging of the PFSA membrane pore structure. The presence of mobile coins and multiple couterions is not considered, but the conductivity of fully ion-exchanged sodium and lithium-form membranes[39] are studied in addition to proton transport.

Theory

Physical Model

In PFSAs, the hydrophobic phase surrounds hydrophilic domains consisting of immobilized sulfonate groups, counterions, and absorbed water.[2] In the fully hydrated state ($\lambda \approx 20$), the hydrophilic domains are locally flat, ribbon-like channels with an average (mean) thickness of 0.85 nm and a width of 2.5 nm.[5, 40-41]

Assuming a realistic physical representation of the aqueous nanodomains is imperative to provide a useful mathematical model. Figure 2 provides this representation. Solvent regions are completely phase

separated from the polymer backbone and sidechains to form lamellar channels with appended ionized sulfonate groups. Hydrophilic sulfur and oxygen atoms of the sulfonate groups are coarse grained as hemispheres. Because neighboring sulfonate groups need not be attached to the same PFSA chain, the amount of backbone between sidechains does not dictate the spacing between sulfonates along the channel. Rather, the anion groups are uniformly distributed along the walls of the channel such that the distance between groups is maximal; electrostatic repulsion between sulfonate groups is minimized. Consequently, water swells the domain isotropically. This representation reduces the hydrophilic lamellar channel into repeating periodic cubic unit cells of dimension l .

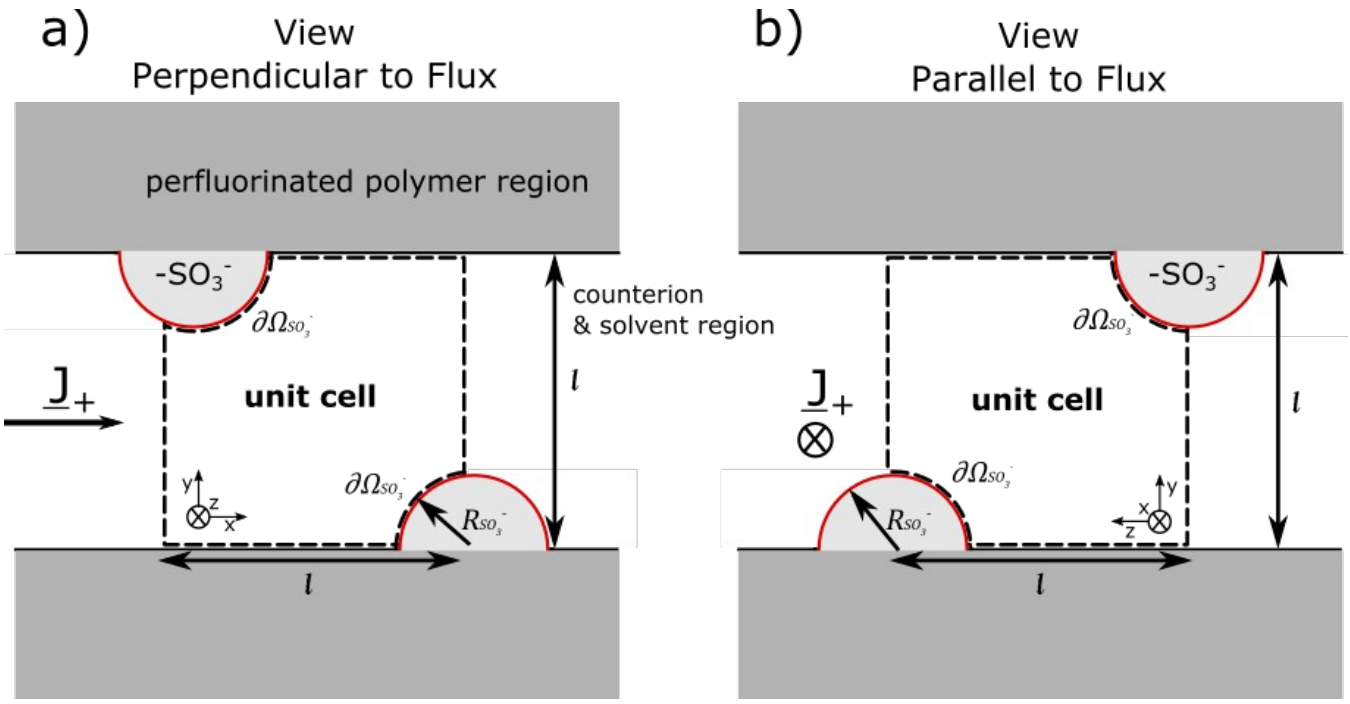

Figure 2. Schematic of the unit cell from (a) direction perpendicular to the direction of flow, i.e. x-y surface of unit cell, and from (b) direction parallel to the direction of cation flux, i.e. y-z surface. $\partial \Omega_{SO_3^-}$ denotes the surface of protruding sulfonate groups. See text for details of notation.

The volume of the aqueous-domain unit cell consists of a single cation of unhydrated radius $R_{+¿}$, λ water molecules each of volume V_w, and four quarters of a sulfonate group with radius $R_{so_3^{-¿}}$ each at alternating corners of the cube. The λ water molecules include free waters and those solvating the ions. The unit cell is bounded by an insulating polymer ceiling and floor (i.e. in the y-direction) and mirrored periodic unit cells on each side (i.e. in the x- and z- directions). Channel thickness of the unit cell with λ = 20 [H_2O/SO_3] is 0.86 nm, close to that experimentally measured.[5, 41]

Water molecules and cations are internal to the system; sulfonate moieties and polymer matrix are external. The membrane is in equilibrium with external water vapor at the overall boundary of the membrane and does not exchange ions with the environment. The chemical potential of water is constant throughout the membrane. Cations are idealized as spheres; hydrated protons exist as hydronium ions.

Mathematical Model

Transport

Transport of cations along the channels is driven by an applied electrostatic potential difference $-\Delta\Phi$ in the *x*-direction. No net current flows in the *y*- and *z*-directions. The cross-section average current density $\langle i \rangle$ across a unit cell of the channel is proportional to the average applied electric field[42]

$$\langle i \rangle = \langle \kappa \rangle \left(\frac{-\Delta \Phi}{l} \right) \quad (1)$$

where $\langle \kappa \rangle$ is the integrated conductivity of the unit cell. The average current density is obtained by averaging of the local current density $\underline{i}$ over a surface of the unit cell normal to the direction of transport. Because the sulfonate anion is immobile, the local current density is due only to the cation flux $\underline{J}_{+¿}$ [42]

$$\underline{i} = ¿ z_{+¿} e \underline{J}_{+¿} \quad (2)$$

where $z_{+¿}$ is the valence of the cation, e is elementary charge, and underbars denote vectors. At constant pressure and temperature and negligible convection, the local flux $\underline{J}_{+¿}$ of cations in the hydrophilic channels is driven by a gradient in the cation electrochemical potential $\tilde{\mu}_{+¿}$ [43-44]

$$\underline{J}_{+¿}(\underline{r}) = -\underline{\underline{u}}(\underline{r}) \rho_{+¿}(\underline{r}) \nabla \tilde{\mu}_{+¿} \quad (3)$$

where $\underline{r}$ is the position vector inside the pore, $\rho_{+¿}$ is the local molecular concentration (i.e. time averaged probability density) of the cation, and $\underline{\underline{u}}$ is the anisotropic, diagonal cation mobility tensor.

$\underline{\underline{u}}$ deviates from the scalar mobility in bulk solution, $u_{+¿}^{\infty}$, due to hydrodynamic-drag tensor

against the domain walls, β ,[45-47] and increased viscosity of the liquid phase, η , around sulfonate groups due to dielectric friction (i.e. resistance of dipole rotation in an electrostatic field)[48] so that

$$u_{i}(r)=u_{i}^{\infty}\beta(r)\frac{\eta^{\infty}}{\eta(r)} \qquad (4)$$

where η^{∞} is the viscosity of the pure solvent. Appendix A: Cation Mobility discusses calculation of β . Einstein's law in the ideal dilute-solution limit (i.e. $\rho_{i}\to 0$) relates cation mobility in bulk aqueous solution to conductivity, κ_{i}^{∞} [49]

$$u_{i}^{\infty}=\frac{\kappa_{i}^{\infty}}{z_{i}e^{2}N_{A}\rho_{i^{\infty}}} \qquad (5)$$

where $\kappa_{i}^{\infty}/\rho_{i^{\infty}}$ is the molar cation conductivity at infinite dilution and N_A is Avogadro's number.

Values of u_{i}^{∞} for studied cations are in Table 1. Proton mobility given by Equation 5 includes both vehicular and Grotthus (i.e. proton hopping) contributions because proton conductivity at infinite dilution occurs by both mechnisms.[3]

Table 1. Cation parameters used in the study.

	H^{+}**	Li^{+}	Na^{+}
R_{i} [Å]**	1.00	0.780	1.02

ΔG^{∞}	[kJ mol^{-1}]†	–432	-510	-411
ΔG^{sat}	[kJ mol^{-1}]‡	-304	-387	-296
u_{i}^{∞}	[s kg^{-1}] x 10^{-11} §	22.6	2.50	3.24
α	[1E-24 cm^3]‖	0.98	0.029	0.179
I	[eV]‖	12.62	5.391	5.139

* All properties based on a hydronium ion except u_{i}^{∞}, which is the dilute solution proton mobility.

** taken from Refs [50], [51] and [52]. † for liquid water $\varepsilon_b = 78$ at 298 K taken from Refs [53], [54], and [52].

‡ for liquid water calculated using Equation 23 in Ref 33, using the parameters listed in this.
§ for liquid water at 298 K taken from Ref [55].
‖ taken from Refs [56] and [57].

At steady state, the divergence of the local flux is zero

$$\nabla \cdot \underline{J}_{i}(\underline{r}) = 0 \tag{6}$$

Boundary conditions for Equation (6 are zero flux at the polymer floor and ceiling of the unit cell ($y = 0, l$), at the interface with the sulfonate groups, $\partial \Omega_{SO_3}$, and, because of symmetry, at the boundary of the neighboring cells that are parallel to the direction of transport ($z = 0, l$

$$\underline{J}_{SO_3^-}(\underline{r}) \cdot \underline{n}_{SO_3^-} = 0 \quad \forall \underline{r} \in \partial \Omega_{SO_3^-} \tag{7}$$

Boundary conditions at the upstream ($x = 0$) and downstream ($x = l$) boundaries are Dirichlet conditions of a fixed potential drop

$$\phi^{us}, \forall \underline{r} \in x = 0 \quad \phi(\underline{r}) = \tilde{\mu}_{i}$$

$$\phi^{us} - e\Delta\Phi, \forall \underline{r} \in x = l \quad \phi(\underline{r}) = \tilde{\mu}_{i} \tag{8}$$

where $\tilde{\mu}_{+¿}^{us}$ is a reference upstream electrochemical potential. $\Delta\Phi$ is set to an applied potential of 10^{-8} V (equivalent to an electric field of 116 V m^{-1} for a unit cell with $\lambda=20$), which is small enough to ensure linearity of the flux with respect to the applied potential but large enough for numerical precision.

Thermodynamics

Numerous molecular interactions in the PFSA aqueous domains dictate the distribution of the cation throughout the channel, including electrostatic interactions between the sulfonate and cation, solvation forces, dispersion and image-charge forces at the interface between the solvent and hydrophobic polymer walls and thermal entropy. Interactions are expressed through the electrochemical potential of the cation, $\tilde{\mu}_{+¿}$,

$$+¿\, e\Phi(\underline{r})+\mu_{fs}(\underline{r})+\mu_{solv}(\underline{r})+\mu_{dsp}(\underline{r})+\mu_{img}(\underline{r}) \qquad (9)$$
$$+¿.(r)+z. \qquad (1)$$

where $\tilde{\mu}_{+¿}^{0}$ is the reference electrochemical potential of the cation, k_B is the Boltzmann constant, T is absolute temperature, Φ is ionic potential, and μ_{fs}, μ_{solv}, μ_{dsp}, and μ_{img} are the excess chemical potentials (i.e. excess free energies) due to ion finite-size, solvation, dispersion, and image charge, respectively. The first two terms in Equation (9) describe ideal-solution behavior, whereas the third term characterizes electrostatics. The final four terms account for ion non-idealities. Each term, except the reference chemical potential, is a function of position inside the pore.

μ_{fs} accounts for the entropy loss by excluding water from regions with high ion concentrations. It is expressed with the widely used local-density Bickermann equation[58-59]

$$\mu_{fs}(\underline{r}) = -k_B T \ln \frac{+¿(\underline{r})}{1-\frac{4}{3}\pi a^3 \rho_¿}} \quad (10)$$

where a is a finite-size parameter. Equation (10 is valid for lattice systems in which the solvent and ion have equal radii. When the ion and solvent are of different size, the choice of a is unclear. The results are relatively insensitive to the choice of a, and here a is set equal to the radius of a water molecule.

Cation-solvation excess chemical potential, μ_{solv}, accounts for the change in solvent potential energy due to dipoles orienting around the cation. Relative permittivity, ε, gauges the amount that dipoles can orient around a cation. Permittivity is extremely heterogeneous across a PFSA membrane nanodomain. Water solvating the sulfonate groups is dielectrically saturated ($\varepsilon = 1.8$) but water separated from the ions has a permittivity of bulk water ($\varepsilon = 78.3$).[8, 33] Relative permittivity of the polymer backbone is 2.1.[60] The dependence of solvent permittivity on $\underline{r}$ is discussed in the next section. Solvation excess chemical potential at $\underline{r}$ is equal to the work to discharge a cation in a reference dielectric plus the work of charging the cation in a dielectric at $\underline{r}$ [52]

$$\mu_{solv} = \int_V dV \int_0^D \frac{D}{\varepsilon \varepsilon_0} - \frac{D}{\varepsilon^\infty \varepsilon_0} dD \quad (11)$$

where V is volume, D is the displacement field of the cation ($D = z_{+¿} e / 4\pi r_{+¿}^2$), ε_0 is vacuum permittivity, and ε^{∞} is the relative permittivity of bulk water, which is the reference dielectric. For a medium in which the permittivity varies slowly over space, the integral with respect to the displacement field was accurately approximated by Bontha and Pintauro as[33]

$$\mu_{solv}(\underline{r}) = -\int_0^{2\pi} d\theta \int_0^{\pi} d\psi \int_{¿}^{\infty} \frac{A}{r_{+¿}^2(\underline{r}) \left(\frac{1}{\varepsilon(\underline{r})} - \frac{1}{\varepsilon^{\infty}} \right)} dr_{+¿} \quad (12)$$

where θ and ψ are spherical angular coordinates, $r_{+¿}$ is the distance to the center of the cation, $R_{+¿}$ is the radius of the cation, and A is a constant. The value of A is determined by interpolating between the solvation free energy in bulk solution, ΔG^{∞} , and the solvation free energy in a dielectrically saturated solution, ΔG^{sat} ,

$$A = ¿ \frac{R_{+¿}}{4\pi} \left(\frac{\Delta G^{sat} - \Delta G^{\infty}}{\frac{1}{\varepsilon^{sat}} - \frac{1}{\varepsilon^{\infty}}} \right) \quad (13)$$

where ε^{sat} is the relative permittivity of a dielectrically saturated solvent. Values of ΔG^{∞} and ΔG^{sat} for different cations are in Table 1. The forms of Equations (12) and (13) are the same as those

given by Bontha and Pintauro[33] except that we explicitly integrate over the volume rather than assume permittivity varies slowly over space. Equation (12) reduces to the solvation excess chemical potential given by Bontha and Pintauro[33] in the limit of $\nabla \varepsilon = 0$. To avoid simultaneously solving Equations (3), (6), (9), and (12), which is a set of coupled integral-differential equations, we approximate μ_{solv} as the linear superposition of the solvation excess chemical potentials due to interactions with the PTFE floor and ceiling of the unit cell, which is only a function of the distance to the boundaries, d_y, and interactions with the sulfonate group, which is only a function of distance to the groups, $d_{SO_3^-}$ as discussed in Error: Reference source not found.

Solvation free energies account for polarization of permanent dipoles whereas van der Waals forces account for induced oscillating polarization of atoms. The dispersion force on a cation is the difference in van der Waals forces acting on a cation from water and from the PTFE polymer walls. The excess chemical potential accounting for dispersion forces, μ_{dsp}, is thus[61]

$$\mu_{dsp}(\underline{r}) = \frac{B}{y^3} + \frac{B}{(1-y)^3} \tag{14}$$

where

$$B = \frac{\pi \alpha_{+} I_{+} I_{+}}{4} \left(\frac{\rho_w \alpha_w I_w}{I_{+} + I_w} - \frac{\rho_T \alpha_T I_T}{I_{+} + I_T} \right) \tag{15}$$

and α, I and $\dot{\rho}$ are the diamagnetic polarizability, first ionization potential, and molecular density. Subscripts $+¿$, w, and T denote the cation, water, and PTFE, respectively. Values of α and I for studied cations are in Table 1. Equation (14) superimposes dispersion forces arising from the unit-cell floor and ceiling (first and second terms, respectively).

μ_{img} accounts for electrostatic interactions felt by an ion near the interface between two media with different dielectric constants. For the case of an aqueous ion adjacent to a water/PTFE interface, the method of image charges and Coulomb's law gives μ_{img} as[62]

$$\mu_{img}(\underline{r}) = \left(\frac{\varepsilon^{\infty} - \varepsilon_T}{\varepsilon^{\infty} + \varepsilon_T}\right) ¿ \; e^2 \frac{z_{+¿^2}}{16\pi\varepsilon^{\infty}\varepsilon_0}\left(\frac{1}{y} + \frac{1}{l-y}\right) \qquad (16)$$

Figure 3 shows the excess chemical potential of solvation, dispersion, and image charges as a function distance from a wall (or sulfonate group for $\overset{SO_3^{-¿}}{\mu_{solv}^{¿}}$). Solvation forces are the dominant excess free energy. Beyond 0.6 nm from the walls, all excess chemical potentials are relatively small.

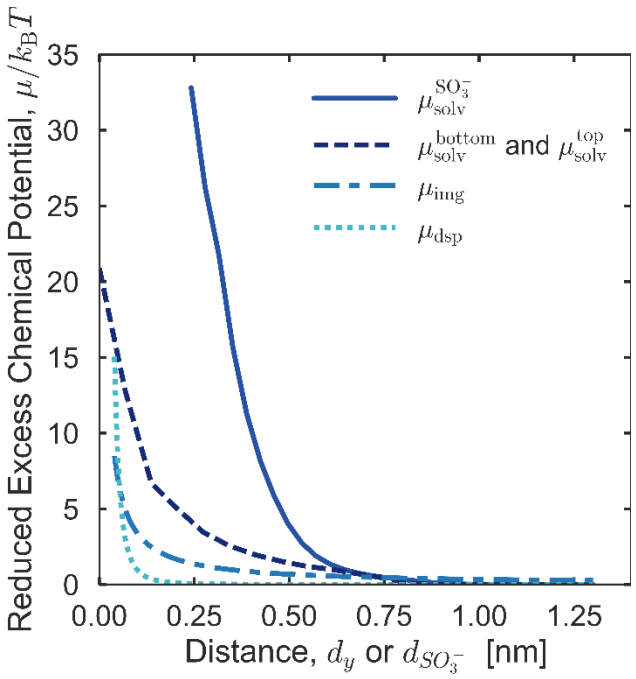

Figure 3. Excess hydronium chemical potentials μ_{solv}^{bottom} and μ_{solv}^{top} (dashed line), μ_{dsp} (dotted line), and μ_{img} (dash-dotted line) as a function of distance from the polymer wall and $\mu_{solv}^{SO_3^-}$ (solid line) as a function of distance from a sulfonate group.

Ionic Potential

Poisson's equation is necessary to close the above system of equations

$$\nabla \cdot \varepsilon(\underline{r}) \nabla \Phi(\underline{r}) = \frac{-e}{\varepsilon_0} z_i \qquad (17)$$

where $+i(\underline{r})$ and $+i\,\rho_i$.

The strong electric field due to the charged sulfonate groups[63] and disruption of the hydrogen-bond network of water due to wall proximity[64] creates variations in ε across the unit-cell domain.

Booth's equation describes how the relative permittivity saturates with increased electric field[63, 65]

$$\varepsilon(\underline{r}) = n^2 + \frac{3\left(\varepsilon^{con}(\underline{r}) - n^2\right)}{\gamma\left|\nabla \Phi(\underline{r})\right|}\left[\frac{1}{\tanh\left[\gamma\left|\nabla \Phi(\underline{r})\right|\right]} - \frac{1}{\gamma\left|\nabla \Phi(\underline{r})\right|}\right] \qquad (18)$$

where

$$\gamma=\left(\frac{5p}{2k_BT}\right)\left(n^2+2\right),$$

n is the bulk refractive index of water, p is the water dipole moment, and ε^{con} is the relative water permittivity before an electric field is applied. ε^{con} is reduced from bulk-water permittivity because the polymer walls disrupt the hydrogen-bonding network of water that causes the high permittivity of bulk water.[64] Water coordinates with neighboring water molecules forming a cluster of radius $R^{\infty}_{cluster}$.[66] At a phase boundary, water coordination is disrupted reducing the cluster radius to $R_{cluster}$.[66] Decreased cluster size reduces permittivity.[66] Lamm et al.[64] show that at 298 K the effect of water confinement on relative permittivity is well approximated as

$$\varepsilon^{con}\left(\underline{r}\right)=17.5\left(1+1.7f\left(\underline{r}\right)^{\frac{1}{6}}+0.5f\left(\underline{r}\right)^{\frac{1}{3}}+f\left(\underline{r}\right)+0.24f\left(\underline{r}\right)^{\frac{1}{2}}\right)+0.8 \tag{19}$$

where $f=\left(R_{cluster}/R^{\infty}_{cluster}\right)^{\frac{1}{3}}$. Error: Reference source not found details calculation of f.

Boundary conditions for Equation (17) are

$$\begin{gathered}0,y,z=0,l\\ ¿\\ SO_3^{-¿}\\ \sigma_{-¿,\underline{r}\in\partial\Omega_¿}-\underline{n}\cdot\varepsilon_0\varepsilon\left(\underline{r}\right)\nabla\Phi\left(\underline{r}\right)\|_{x=0},x=l\\ \underline{n}\cdot\varepsilon_0\varepsilon\left(\underline{r}\right)\nabla\Phi\left(\underline{r}\right)=¿\end{gathered} \tag{20}$$

and

$$\Phi\left(\acute{r}\right)=\Phi\left(\acute{r}\right)\big|_{x=0}-\Delta\Phi,x=l \tag{21}$$

where $\underline{n}$ is the unit normal vector to the boundary and $\sigma_¿^{-¿}$ is the charge density on the sulfonate group assuming that the negative charge distributes uniformly on the surface of the representative

hemisphere, $\begin{matrix} SO_3^{-¿} \\ 2\pi R_¿ \\ -¿=e/¿ \\ \sigma_¿ \end{matrix}$. The first boundary condition specifies zero current through the insulating polymer and perpendicular to the channel. The second condition is Gauss's law accounting for the charge of the sulfonate groups. Third and fourth boundary conditions impose periodicity of the unit cells. Because neighboring unit cells are the mirror images of each other, the boundary conditions are similarly mirrored at the boundaries (e.g. the lower-right corner of the downstream boundary in Figure 2a maps to the upper-left corner of the upstream boundary). Figure S1 displays boundary conditions.

Numerical Method

Equations (6), (9), and (17) were solved simultaneously using COMSOL Multiphysics 5.1 (COMSOL, Inc., Palo Alto, CA) on the 3-D geometry portrayed in Figure 2. The mesh consisted of tetrahedrals with triangular elements at the boundaries. 30,153 to 23,893 domain elements were used with 2,680 to 2,558 boundary elements; the number of elements increased with increasing water content. Resulting 173,996 to 138,148 degrees of freedom for the coupled physics were solved using the MUMPS general solver using Newton-Raphson iteration to resolve nonlinearities. Convergence was achieved for a relative tolerance of $1x10^{-8}$.

Results and Discussion

Nanoscale Physics

Aqueous Domain Free Energies

The negatively charged sulfonic acid groups impose strong electrostatic fields throughout the unit cell. Figure 4 and S2 in supporting information show 2D intensity maps on the x-y surface of the unit cell to illustrate the impact of the resulting field. Figure S2a shows the electrostatic field leads to a sharp

decline in ionic potential near the sulfonate groups. Figure 4a shows that near the sulfonate groups the electrostatic field combined with wall confinement disrupts the bonding structure of water resulting in a lower relative permittivity than that of bulk water (i.e. ~78). The strong electric field orients the water surrounding the sulfonate groups causing dielectric saturation of the water that is solvating the sulfonates. Conversely, water near the center of the channel exhibits bulk-like permittivity.

Figure 4b shows the cation concentration, $\rho_{+¿}$ (normalized by the average cation concentration in the unit cell, $\rho_{+¿}^{0} = 1/V_{tot}$, where V_{tot} is the unit-cell volume). Figure 5 shows the cation concentration between two adjacent sulfonate groups at $\lambda = 9$ (solid line) and $\lambda = 4$ (dot-dashed line). Cations are distributed throughout the channel with the highest concentrations near the surface of the sulfonate groups and near the midpoints between groups. By plotting the electrostatic and solvation free energies (dashed and dotted lines for $\lambda = 9$ and 4, respectively), Figure 5 shows that the distribution of cations in the channel is due to competition between electrostatic and solvation forces resulting in a balance of free energies, consistent with the work of Pintauro and coworkers.[33] Electrostatic free energy is most favorable when aqueous cations are close to the negatively charged sulfonate groups. Conversely, solvation free energy is most favorable when aqueous cations are outside the solvation shell of the sulfonate groups. The strong electrostatic fields of the sulfonate group cause cations within the solvation shell of the sulfonates to dehydrate partially. At low water contents, there is insufficient water to hydrate the cations fully, which decreases the solvation energy at the center of the channel, and results in the dominance of electrostatic interactions. Figure S3 shows that as water content decreases, the free energy balances from solvation to electrostatic and increases the fraction of

cations associated with sulfonate groups. The predicted fraction of cations associated with sulfonate groups shows excellent agreement with atomistic simulations.[26, 29-30]

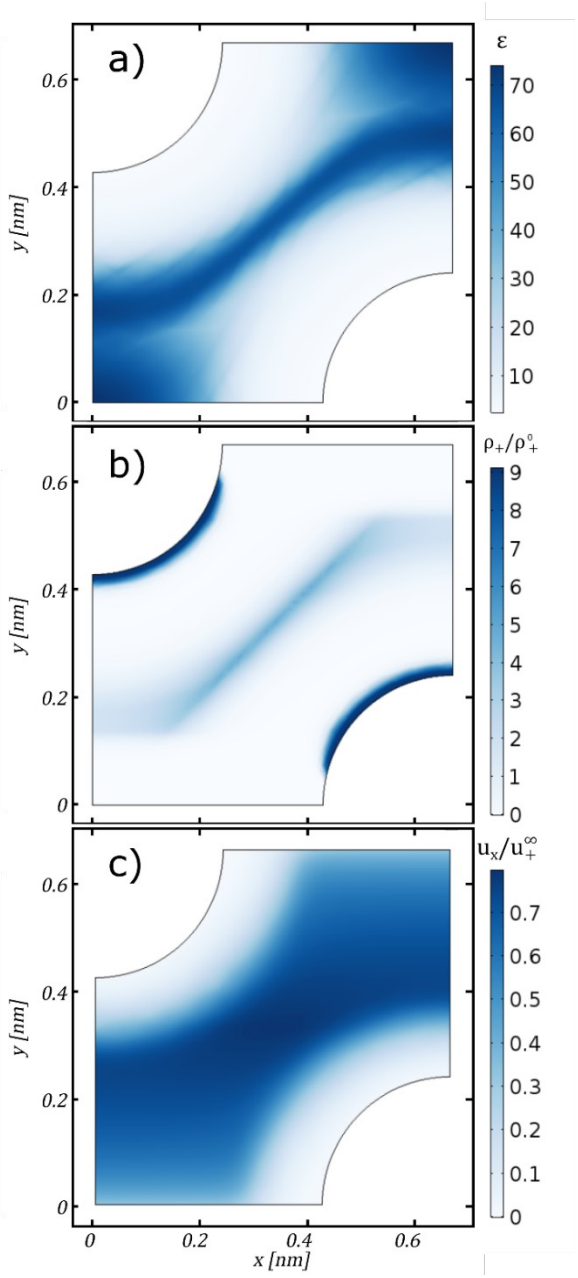

Figure 4. 2D intensity map of the x-y surface of the unit cell for protonated membrane at λ = 9 [H_2O/SO_3] of (a) water relative permittivity, ε, (b) hydronium probability density normalized by the average unit cell

probability density, ρ_{+}/ρ_{+}^{0}, and (c) the x-component of hydronium mobility, reported as u_x/u_{+}^{∞}, colored from white (light) to blue (dark) to represent low to high values.

Figure 6 shows that the radial distribution function (RDF) of the cation with respect to the center of the sulfonate group displays three peaks, also consistent with molecular dynamics simulations.[26] Supporting Information gives details of the RDF calculation. The first peak, located at 2.4 Å, is caused by partially desolvated cations that form contact-ion pairs with the sulfonate groups (Inset a). The second peak located near 4-6 Å is caused by solvated cations that separate from the sulfonate groups and reside near the center of the channel (Inset b). The third peak, near 5.5-9 Å, arises from cations that form ion pairs with opposing sulfonate groups (Inset c).

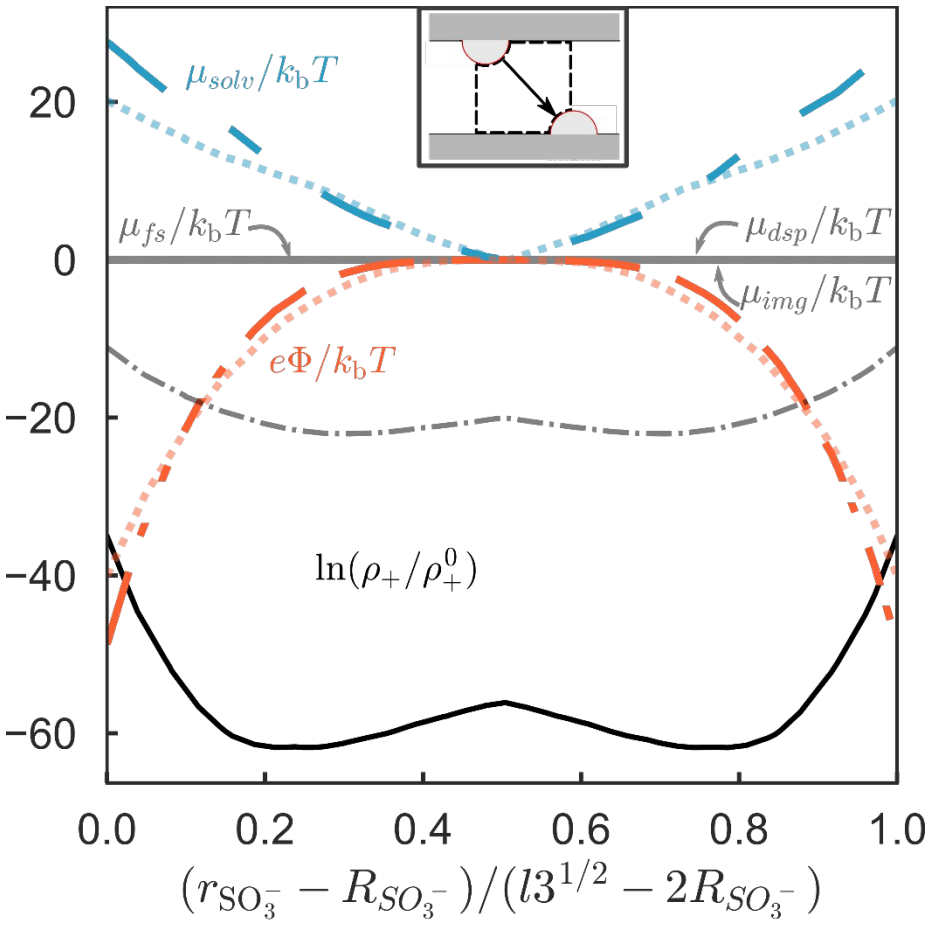

Figure 5. $+¿^{0}$ $+¿/\rho_{¿}$ $\rho_{¿}$ $ln\ ¿$ (denoted solid and dot-dashed lines), $e\Phi/k_bT$ (denoted dashed and dotted lines), and μ/k_bT (denoted solid lines for image charge, dispersion and finite size effects and dashed and dotted lines for solvation) terms evaluated on a diagonal between two opposing sulfonate groups at $\lambda=9$ and 4 [H2O/SO3], respectively, for a protonated membrane. The distance is normalized between 0 and 1. The insert is a simplification of Figure 2a with an arrow indicating the diagonal between the opposing sulfonate groups. μ_{ex} terms are referenced to the midpoint between the opposing sulfonate groups.

Positions of the second and third peaks of the RDF in Figure 6 shift depending on membrane water content. As water content decreases from $\lambda=15$ (solid line) to $\lambda=9$ (dashed line) and $\lambda=4$

(dotted line), the unit cell shrinks; the distance between sulfonate groups decreases. The distance between a sulfonate group and cation contact pairs of opposing sulfonate groups decreases; the third RDF peak shifts inward. Similarly, as water content decreases, the distance between a sulfonate group and the center of the channel decreases causing the second RDF peak to shift inward. The radial distribution function specifies cation distribution to the furthest extent of the cubic unit cell (i.e. $3^{1/2}l$).

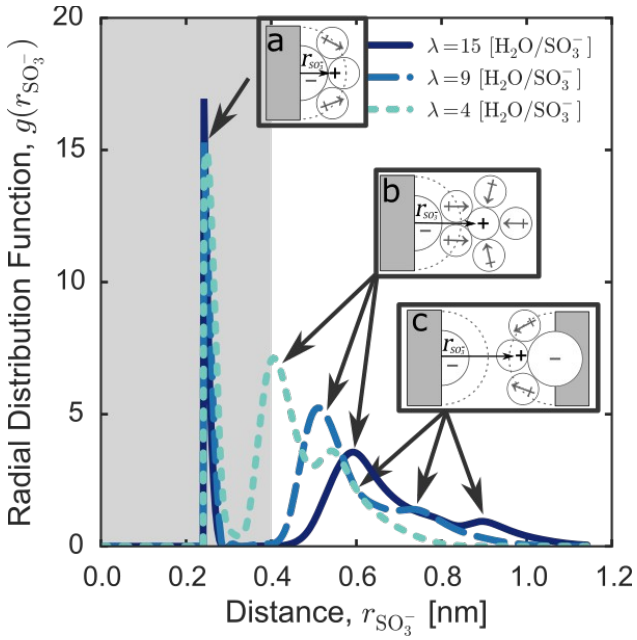

Figure 6. Hydronium RDF with respect to the center of a sulfonate group at water content of λ = 4 (dotted line), 9 (dashed line), and 15 [H_2O/SO_3] (solid line) for an 1100 EW membrane. The region shaded dark grey locates the first solvation shell of sulfonate. Schematic inserts depict the water dipole structure (↠) around the aqueous cation center of charge (+) with respect to a sulfonate group (–) for each peak in the RDF; solid lines denote the hard-sphere radius of the species, dotted lines denote the first solvation shell of the sulfonate group. Arrows indicate the distance $r_{SO_3^-}$. Grey region denotes the polymer. Only water dipoles solvating the cation are shown.

Aqueous Domain Transport

The strong electrostatic fields around the negatively charged sulfonate groups increases water viscosity due to dielectric friction, as Figure S2b shows. Viscosified water corresponds to water molecules that solvate the sulfonate groups. Conversely, water near the center of the channel is more bulk-like. This is qualitatively consistent with prior work of Yang and Pintauro[32, 67], but they attributed increased solvent viscosity directly to ion concentration effects. Figure 4c illustrates that increased water viscosity combined with increased hydrodynamic drag near the walls significantly reduces aqueous cation mobility throughout the channel. Decreased mobility near the walls causes the local conductivity to be maximum near center of the channel, as Figure S2c shows. Cation conductivity is facilitated by solvated cations transporting along the center of the channel.

Figure 7 shows unit-cell conductivity as a function of water content. Ideal-solution conductivity at the average concentration of the unit cell, $\kappa_{c_+^\infty}$ (dotted line), decreases with increasing water content because water dilutes the number of charge carriers. Dielectric friction caused by the electric field emanating from the sulfonate groups reduces conductivity (dashed line, calculated using Equation (3) with $\underline{\underline{u}} = \underline{\underline{I}} u_{c_+^\infty}\eta/\eta^\infty$ where $\underline{\underline{I}}$ is the identity tensor). There is a maximum in the dielectric friction-

corrected cation conductivity at $\lambda=4$ because below this water content increasing water content decreases the fraction of immobile, bound cations, which increases conductivity. Above this water content, dilution effects dominate and conductivity decreases with increasing water content. Average domain conductivity, $\langle\kappa\rangle$, includes the resistance from the hydrodynamic drag on the cations due to confinement (solid line, calculated using Equation (3) with $\underline{u}$ given by Equation (4)). Nanoscale factors reduce conductivity from the ideal-solution limit the most at low water contents. The resulting domain conductivity changes relatively little with water content (~26% difference between the smallest and largest values of $\langle\kappa\rangle$ versus ~520% difference for κ_{+}^{∞}). Figure S4 shows that although nanoscale resistance depends on water content, it is relatively insensitive to how the domains swell (anisotropic vs. isotropic swelling).

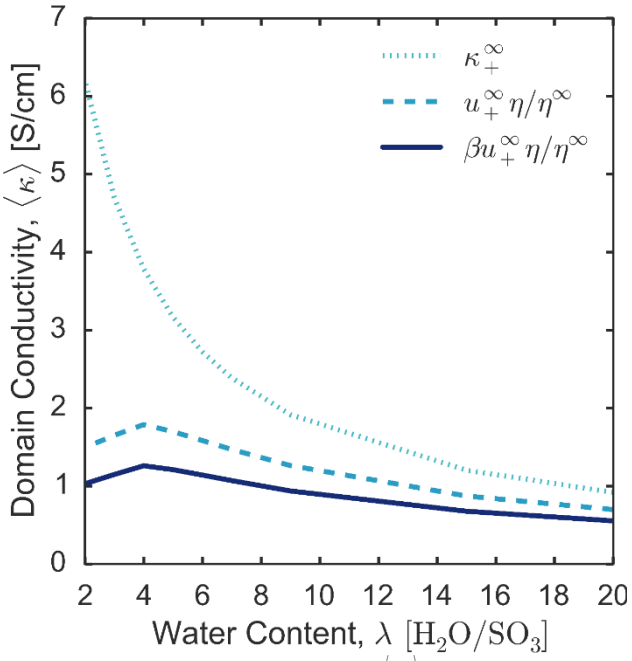

Figure 7. Average hydronium conductivity in a domain, $\langle\kappa\rangle$, as function of water content, λ,

calculated from κ_{+}^{∞} at the average unit-cell concentration (dotted line), from Equation (3) with $u=u_{+}$ κ/κ^{∞} (dashed line), and from Equation (3) with $u=\beta_{\parallel}u_{+}$ κ/κ^{∞} (solid line).See Appendix A for calculation of $\beta_{\parallel}$.

Impact of Side-Chain Size

The molecular composition of the PFSA sidechain (e.g. the number of fluorocarbon or fluoroether groups) influences the partial charge on molecular groups neighboring sulfonates[29] and, consequently, the overall membrane conductivity.[4, 68] Charge delocalization decreases the fraction of cations associated with the sulfonate groups and increases membrane conductivity.[29, 28, 68-69] Charge delocalization is modeled qualitatively by increasing the size of charged hemisphere, $R_{SO_3^-}$, to account for the increase of the effective size of the negatively charged moiety which include the sulfonate group and some amount of polymer sidechain over which the negative charge is delocalized. Figure 8 reports average domain hydronium conductivity (solid line) and the fraction of hydronium ions associated with sulfonate groups (dashed line) at $\lambda=9$ as a function of $R_{SO_3^-}$. Delocalization of the negative sulfonate-group charge (with increasing $R_{SO_3^-}$) decreases the fraction of cations associated with sulfonate groups. Charge delocalization lessens the electrostatic free-energy benefit of cation/sulfonate group contact pairs, which increases the number of solvated cations. Decreasing the fraction of cations associated with sulfonate groups causes conductivity to increase up to a point where most of the cations

are completely dissociated. Additional delocalization of the negative charge causes the conductivity to decrease slightly because the sidechains create physical obstacles to transport.

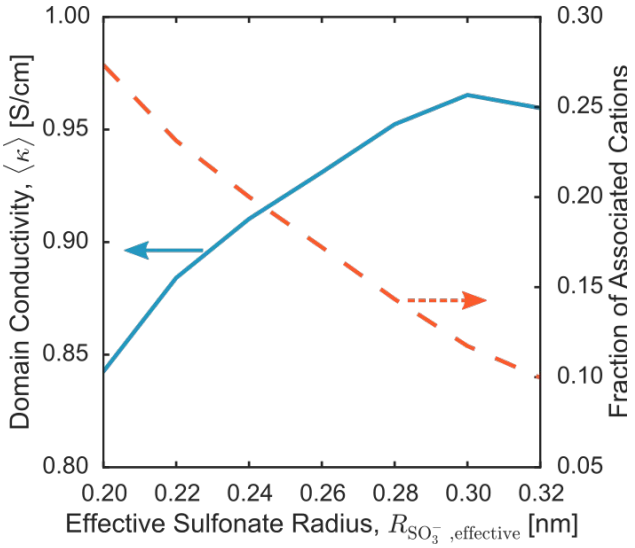

Figure 8. Hydronium conductivity (solid line, left axis) and fraction of cations within the radius of association (4 Å) of sulfonate groups (dashed line, right axis) at λ = 9 [H_2O/SO_3] as a function of the size of the negatively charged side-chain moiety.

Macroscale Physics

The unit-cell model for PFSA membranes captures the essence of known behavior at the nanoscale.[4] We now extend the aqueous-domain results to predict macroscopic transport properties in PFSAs. Modeling macroscopic properties is challenging because the aqueous-domain model only accounts for phenomena at the nanoscale. It does not account for transport across a network of connected domains. A bundle-of-tubes model describes transport through the medium. The effective macroscopic conductivity κ^{eff} is[70]

$$\kappa^{eff} = \frac{\varphi}{\tau^2}\langle\kappa\rangle \tag{22}$$

where κ^{eff} is the effective macroscopic conductivity of the membrane, τ is the tortuosity of the network, and φ is membrane hydrophilic volume fraction, which is taken as the combined volume fraction of water and sulfonate groups

$$3\pi \frac{R_{SO_3^-}^3}{V_w \lambda + \frac{EW}{N_A \hat{\rho}_{poly}}} \qquad (23)$$

$$V_w \lambda + \frac{4}{\text{¿}}$$

$$\varphi = \text{¿}$$

where $\hat{\rho}_{poly}$ is the mass density of dry polymer (~ 2 g/cm^3)[71] and EW is the equivalent weight of the membrane (g polymer/mole of sulfonate groups).

Varying the cation type of the membrane ("cation form") and polymer chemistry changes τ and $\langle \kappa \rangle$ in Equation (22) independently. For example, for the same membrane chemistry and water content, tortuosity is assumed independent of cation type. Specifying $\langle \kappa \rangle$ with the nanoscale model and fitting φ / τ^2 to conductivity of one cation-form membrane predicts resistance of other cation-forms. Figure 9a shows experimental (symbols) and predicted (lines) membrane conductivity, κ^{eff}, for sodium and proton membranes with φ / τ^2 fit using conductivity of lithium membrane at the same water content. Agreement is good. Proton-form membranes have the highest conductivity because hydronium cations readily dissociate from the sulfonate group and have the largest mobility. Conductivity of lithium- and sodium-form membranes are similar; sodium ions have a higher bulk mobility than lithium ions but are hindered in the domains because they are more likely to form ion pairs with sulfonate groups.

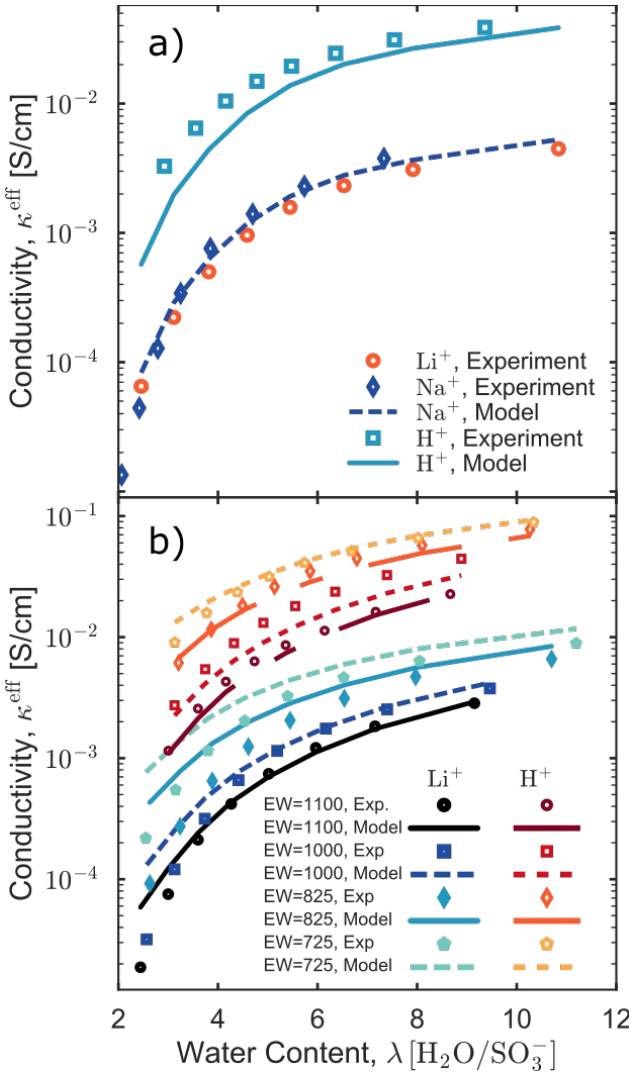

Figure 9. Experimental (symbols) and predicted (lines) conductivity of (a) Nafion membrane (1100 g/mol SO_3 EW) conductivity for lithium- (circles), sodium- (diamonds), and proton-form (squares) membranes and (b) 3M membrane with EWs of 1100 (circles), 1000 (squares), and 825 (diamonds), and 725 g/mol SO_3 (pentagons) in lithium- (blue) and proton-form (red) as a function of water content. Lines are model predictions (Equation (22)).

Additionally, conductivity of different membrane chemistries further validates the model. We assume that network tortuosity is solely a function of the hydrophilic-phase volume fraction and distribution (i.e. $\tau(\varphi)$) and that aqueous domain-scale conductivity is entirely a function of the local water content, cation form, and pore geometry (i.e. $\langle\kappa\rangle(\lambda)$). The effect of network tortuosity and aqueous domain-scale conductivity is separated by changing the amount of hydrophobic backbone in the polymer per

sulfonate group (i.e. EW) and by measuring the conductivity of the membranes at different water contents. To account for how tortuosity varies with hydrophilic volume fraction we use the empirical expression[72]

$$\tau = e^{\frac{k}{2}\left(\frac{1}{\phi}-1\right)} \tag{24}$$

where k is a fitting parameter. Substitution of Equation (24) into Equation (22) specifies the effective macroscopic conductivity at a given water content and membrane chemistry. k is 0.93, which was fit so membrane conductivity from Equations (22) and (24) matched measured conductivity of a lithium-form membrane at 90% relative humidity (i.e. at $\lambda = 9$). k was taken constant for all EW membranes in lithium- and proton-form. Figure 9b shows that predicted membrane conductivity from Equation (22) (lines) agrees well with measured conductivity (symbols) for both lithium and proton membranes as a function of water content across a range of equivalent weights. The membrane conductivity increases with decreasing EW at the same water content because the hydrophilic volume fraction increases, thereby lowering network tortuosity.

Discrepancy between theory and experiment shown in Figure 9 results from the breakdown in the assumption that tortuosity is exclusively a function of water content. Hydrophilic domain morphology (i.e. locally flat domains or inverted micelles) and related domain connectivity depend slightly on water content and cation form rather than solely on water volume fraction.[4, 24] Furthermore, any domain coalescence or related significant structural changes are not considered

Because Equation (22) explicitly relates transport parameters at the nanoscale ($\langle \kappa \rangle$) and mesoscale (ϕ and τ) to macroscale conductivity, the influence of each length scale is

deconvoluted. The ideal-solution proton conductivity, $\kappa_{i}^{+,\infty}$, at the average concentration of the unit cell, is the upper limit (as defined by Equation (5)). Figure 10 shows the calculated ideal-solution conductivity as a function of water content (dotted line). $\kappa_{i}^{+,\infty}$ decreases with hydration because water dilutes the proton charge carriers. The dashed line in Figure 10 is the proton domain-scale conductivity, $\langle \kappa \rangle$, which is equivalent to the solid line in Figure 6. The difference between the dotted and dashed lines represents the conduction losses due to cation interactions with the polymer matrix and sulfonate side groups. $\langle \kappa \rangle$ is relatively constant with water content because the effect of charge carrier concentration is countered by proton/polymer interactions at lower water content that reduce conductivity. Guided by Equation (22), including the resistances imparted by ϕ (dot-dashed line) and τ (solid line) further reduces the conductivity. The solid line is the measured macroscopic conductivity of an 1100 EW 3M PFSA proton-form membrane, as shown in Figure 9b. Designing polymers that mitigate these interactions may offer an avenue to improve macroscopic conductivity (e.g., delocalization of sidechain charge). However, domain-scale interactions are not the only factors controlling macroscopic conductivity. Network tortuosity and the volume fraction of the conductive phase also dramatically impact conductivity. The importance of the network-level effects of tortuosity and conductive-phase volume fraction explains the success of efforts to increase conductivity by decreasing the hydrophobic volume fraction of the polymer[73] (e.g., lower EW) and reducing the tortuosity.[74-75]

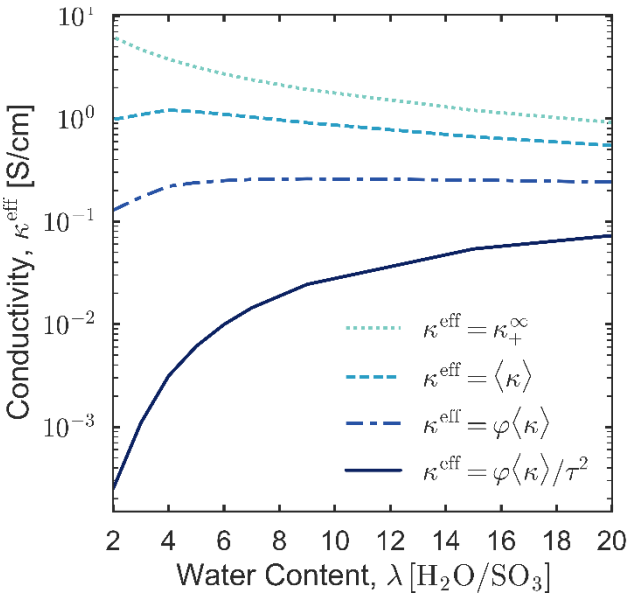
Conductivity, κ^{eff} [S/cm]
10^{1}
10^{0}
10^{-1}
10^{-2}
10^{-3}
2
4
6
8
10
12
14
16
18
20
Water Content, $\lambda\,[\mathrm{H_2O/SO_3}]$
$\kappa^{\mathrm{eff}} = \kappa_{+}^{\infty}$
$\kappa^{\mathrm{eff}} = \langle\kappa\rangle$
$\kappa^{\mathrm{eff}} = \varphi\langle\kappa\rangle$
$\kappa^{\mathrm{eff}} = \varphi\langle\kappa\rangle/\tau^{2}$

Figure 10. Proton-form membrane conductivity as a function of water content at the conductive ideal solution limit at the concentration of the unit cell, κ_{i}^{∞} (dotted line), with the model conductivity from Equation (22), $\langle\kappa\rangle$ (dot-dashed line), with the model conductivity from Equation (22) and accounting for the hydrophilic volume fraction, $\varphi\langle\kappa\rangle$ (dashed line), and with the model conductivity and accounting for the hydrophilic volume fraction and network tortuosity, $\varphi\langle\kappa\rangle/\tau^{2}$ (solid line).

Conclusions

A mean-field, local-density model of ion transport and distribution inside hydrophilic aqueous domains of PFSA membranes was developed and validated. The model adopts an experimentally consistent 3D geometry and accounts for solvation, electrostatic, image charge, dispersion, and finite-size free energies in addition to dielectric friction and wall confinement. The simple macroscale model up-scales the nanoscale model to predict macroscopic conductivity by accounting for the volume fraction and tortuosity of the conductive domains.

Membrane conductivity is facilitated by the movement of solvated cations inside PFSA hydrophilic domains. The fraction of solvated cations is governed by a competition between electrostatic attraction between the cation and negatively charged polymer sulfonate moieties and cation solvation energy. The balance between these two free energies can be varied, for example, by changing sidechain chemistry to delocalize the negative charge on the sidechains, which decreases the fraction of cations binding to the sulfonate groups and increases conductivity.

Aqueous microscale conductivity is relatively constant with water content due to the competition of charge-carrier concentration, which increases conductivity with decreasing water content, and cation solvation, which increases conductivity with increasing water content. Macroscale conductivity increases with increased water content because membrane transport is strongly affected by the tortuosity of the network, which decreases with increasing water content. Addressing transport limitations at both the nano- and network-scales offer avenues to improve membrane performance. Conversely, focus on

optimizing and exploring transport at a single lengthscale without regard for the other may not be fruitful. The model developed here provides a framework to understand the root causes of ion-transport resistances in ion-conductive polymers.

Notation

Roman

A	slope of solvation energy with respect to the inverse of the dielectric constant, J mol^{-}
a	finite size parameter, m
B	constant used in Equation (14)
D	displacement field, C m^{-2}
d	distance, m
e	elementary charge, 1.602E-19 C
EW	equivalent weight of polymer, g/mol (SO_3)
f	fraction of sphere remaining after being intersected by a wall and/or sulfonate groups
ΔG	change in energy due to solvation with a reference to solvation in a vacuum, J mol^{-1}
g	radial distribution function
I	first ionization potential
$\underline{\underline{I}}$	identity matrix
i	ionic current density, A m^{-2}
J	diffusive flux, mol m^{-2} s^{-1}
l	Length of the unit-cell, m
k	fitting parameter in Equation (24)
k_B	Boltzmann Constant, 1.381E-23 m^2 kg s^{-2} K^{-1}
n	refractive index of water at 298 K, 1.330
$\underline{n}$	unit normal vector
N_A	Avogadro number, 6.022E23 molecules mol^{-1}
p	dipole moment of water, 6.17E-30 C m
R	radius, m

r	distance to point, m
$\underline{r}$	position vector, m
T	absolute Temperature, K
u	mobility, s kg^{-1}
V	molecular volume
z	valance

Greek

α	diamagnetic polarizability
β	hydrodynamic mobility correction
γ	constant used in Equation (18)
ε	relative permittivity
ε_0	Vacuum permittivity, 8.854E-12 F m^{-1}
κ	conductivity, S cm^{-1}
η	Viscosity of water, cP
λ	water content, mole H_2O (mole SO_3)$^{-1}$
$\tilde{\mu}$	electrochemical potential, J $molecule^{-1}$
ρ	molecular concentration
$\acute{\rho}$	molecular density
$\hat{\rho}_{poly}$	Polymer mass density, 2 g m^{-3} [71]
$-¿$ $\sigma_¿$	surface charge density, C m^{-2}
τ	square-root of tortuosity
τ_d	Debye dielectric relaxation time for water, 0.82E-11 s from Ref [76]
$\Delta\Phi$	applied ionic potential, 1E-8V
Φ	ionic potential, V
φ	hydrophilic phase volume fraction
$\langle \ldots \rangle$	domain average

Subscripts

$+¿$	cation

$\parallel$	parallel to direction of diffusion
$\perp$	perpendicular to direction of diffusion
cluster	cluster of water molecules over which short range interactions are important ($R_{cluster}^{\infty}$ = 5.91E-10 m from Ref [64])
dsp	dispersion
fs	finite size
img	image charge
S	Cation type
$-SO_3^-$	sulfonate group
solv	solvation
T	PTFE (α_T = 1.97E-24 cm^3, I_T = 13.2 eV, from Ref [77], ρ_T = 0.0440 mol cm^{-3} from Ref [56], ε_T = 2.0 from Ref [60])
tot	accounting for all the unit cell
w	water (V_w = 2.993E-29 m^3 molecule^{-1}, α_w = 1.45E-24 cm^3, I_w = 12.62 eV, ρ_w = 0.0554 mol cm^{-3} R_w = 1.38 Å from Ref [56])
x	x-component of vector
y	with respect to top or bottom of unit cell

Superscripts

0	reference
∞	in solution at infinite dilution (η_∞ = 0.8903 cP from Ref [76], ε_∞ = 78.3[33])
bottom	bottom of the unit cell
con	parameter including confinement but not electrostatic effects
eff	effective macroscopic property for the membrane
hf	high frequency (ε^{hf} = 5.2 from Ref [76])
sat	saturated
$-SO_3^-$	sulfonate group
top	top of the unit cell

us upstream side of the unit cell

*The distance of closest approach between the sulfonate group and water molecule, $SO_3^{-i} + R_{H_2O}$ R_i, is the location of the first peak of the water radial distribution function (RDF) with respect to sulfur.[30] SO_3^{-i} R_i is specified by subtracting the hard sphere radius of water.

Appendix A: Cation Mobility

The Stokes-Einstein equation predicts that ion mobility varies inversely with solvent viscosity, which provides the basis for the $\eta^\infty/\eta(\underline{r})$ correction to mobility in Equation (4). Yang and Pintauro corrected the solvent viscosity based on increased ion concentration.[32, 67] We account for increased water viscosity due to dielectric friction of the sulfonate groups, consistent with nonequilibrium statistical-mechanics calculations.[8, 32, 67] Hubbard determined that the increase in η due to the slower relaxation of dipoles in an electric field to be[48]

$$\eta(\underline{r}) = \eta^\infty \left[1 + \frac{\tau_d}{16\pi\eta^\infty} \left(\varepsilon^\infty - \varepsilon^{hf} \right) \left| \nabla \Phi \right|^2 \right] \quad (1A)$$

where τ_d is the Debye dielectric relaxation time, and ε^∞ and ε^{hf} are the unperturbed and high-frequency dielectric constants of the solvent, respectively.

Because the fraction of bulk mobility due to hydrodynamic drag parallel to a wall, $\beta_\parallel$, and perpendicular to wall, $\beta_\perp$, are different $\underline{\underline{\beta}}$ is an anisotropic, diagonal tensor

$$\underline{\underline{\beta}}(\underline{r}) = \begin{bmatrix} \beta_{\parallel} & 0 & 0 \\ 0 & \beta_{\perp} & 0 \\ 0 & 0 & \beta_{\parallel} \end{bmatrix} \tag{2A}$$

$\beta_{\perp}$ has an exact solution effectively estimated as[45]

$$\begin{array}{l} R_{+¿} \\ \frac{d_y}{¿} \\ ¿ \\ R_{+¿} \\ \frac{d_y}{¿} \\ ¿ \\ R_{+¿} \\ \frac{d_y}{¿} \\ ¿ \\ R_{+¿} \\ \frac{d_y}{¿} \\ ¿ \\ ¿ \\ 6¿ \\ ¿ \\ 6¿ \\ \beta_{\perp} \approx ¿ \end{array} \tag{3A}$$

where d_y is the scalar distance from the center of the cation to the nearest wall (i.e. $y' = y$ or $¿ l - y$). $\beta_{\parallel}$ is estimated as[47]

$$R_{+¿+d_y}$$ (4A)

$$\frac{R_{+¿}}{¿}$$

¿

¿

¿

$$R_{+¿+d_y}$$

$$\frac{R_{+¿}}{¿}$$

¿

¿

¿

$$R_{+¿+d_y}$$

$$\frac{R_{+¿}}{¿}$$

¿

¿

¿

¿

¿

¿

¿

$$R_{+¿+d_y}+\frac{1}{8}¿$$

$$\frac{R_{+¿}}{¿}$$

$$\beta_{\parallel}\approx 1-\frac{9}{16}¿$$

Appendix B: Solvation Energy Calculation

To avoid simultaneously solving Equations (3), (6), (9), and (12), which is a set of coupled integral-differential equations, we approximate μ_{solv} as the linear superposition of the solvation excess chemical potentials due to solvation interactions with the PTFE floor and ceiling of the unit cell, μ_{solv}^{top} and μ_{solv}^{bottom}, respectively, and with the nearest sulfonate group, $\overset{SO_3^{-¿}}{\mu_{solv}^{¿}}$,

$$\mu_{solv}(\underline{r})\approx \mu_{solv}^{top}(\underline{r})+\mu_{solv}^{bottom}(\underline{r})+\overset{SO_3^{-¿}(\underline{r})}{\mu_{solv}^{¿}}$$ (1B)

μ_{solv}^{top} and μ_{solv}^{bottom} are solutions to Equations (12) and (13) for a system with an aqueous cation a distance d_y from a semi-infinite polymer wall ($d_y = y$ and $l - y$ in μ_{solv}^{top} and μ_{solv}^{bottom}, respectively) with a relative permittivity of PTFE, ε_T, as shown in Figure 11a. Because of confinement, ε is slightly lower than ε^{∞} close to the walls. μ_{solv}^{top} and μ_{solv}^{bottom} are each functions only of y and $l - y$, respectively. $\mu_{solv}^{SO_3^{-i}}$ is the solution to Equations (12) and (13) for a second system with a single negatively charged sulfonate group and an aqueous cation a distance d_i from the sulfonate, as shown in Figure 11b. The sulfonate group with the charge uniformly distributed on the surface of the hemisphere causes a displacement field

$$D = e / 2\pi r_i^2 \qquad \text{(2B)}$$

for $y > 0$ where r_i is the distance to the center of the sulfonate group. The displacement field causes the solvent to saturate dielectrically around the appended sulfonate ion, as discussed in the next section. To avoid double counting the effect of the polymer wall in μ_{solv} by both μ_{solv}^{top} or μ_{solv}^{bottom} and $\mu_{solv}^{SO_3^{-i}}$, the relative permittivity of the wall (i.e. $y < 0$) is ε^{∞} in the evaluation of $\mu_{solv}^{SO_3^{-i}}$,

which is a function only of $d_{SO_3^-}$. Equation 1B makes μ_{solv} a function only of $d_{SO_3^-}$ and y.

In the evaluation of μ_{solv}^{top}, μ_{solv}^{bottom}, and $\mu_{solv}^{SO_3^-}$, Equation (12) was computed using midpoint integration in 3D with $8\text{x}10^6$ grid points spaced approximately 3 pm apart extending 0.6 nm from the cation in the x- and z-directions and 0.6 nm in the + y-direction for values of y from 0 to 1.2 nm in increments of 0.1 nm with linear interpolation used for intermediate values of y.

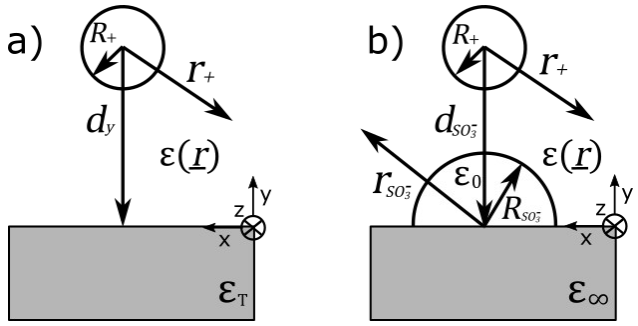

Figure 11. Representation of systems used to calculate the pairwise excess chemical potentials. (a) μ_{solv}^{wall} and (b) $\mu_{solv}^{SO_3^-}$ where the circle and semicircle represent the cation and sulfonate, and the shaded region represents polymer walls. Arrows indicate distances.

Appendix C: Determination of the Dielectric Constant

From simple geometric arguments, the fraction f_j of a sphere of radius R_i remaining after being intersected by each j sulfonate groups or wall a distance d_j from the surface of the sphere is

$$f(\underline{r}) = 1 - \sum_{j}^{¿} \; ¿ \; all\, SO_3^{-¿} \frac{\left(R_i - d_j(\underline{r})\right)^2 \left(3R_i - d_j(\underline{r})\right)}{4R_i^3} \tag{1C}$$

for all $d_j \leq R_i$.

Acknowledgements

This work was funded by the Fuel Cell Technologies Office, Office of Energy Efficiency and Renewable Energy of the U. S. Department of Energy under contract number DE-AC02-05CH11231 and by a National Science Foundation Graduate Research Fellowship under Grant No. DGE 1106400. The authors thank Shouwen Shi for providing experimental conductivity data.

Supporting Information Description

Nanoscale boundary conditions, calculations details of the RDFs, validation against atomistic simulations, and intensity plots of ionic potential, conductivity, and viscosity at the nanoscale (PDF).

References

1. Weber, A. Z.; Borup, R. L.; Darling, R. M.; Das, P. K.; Dursch, T. J.; Gu, W.; Harvey, D.; Kusoglu, A.; Litster, S.; Mench, M. M., et al. A Critical Review of Modeling Transport Phenomena in Polymer-Electrolyte Fuel Cells. *J. Electrochem. Soc.* **2014**, *161*, F1254-F1299.

2. Mauritz, K. A.; Moore, R. B. State of Understanding of Nafion. *Chem. Rev.* **2004**, *104*, 4535-4586.

3. Kreuer, K.-D.; Paddison, S. J.; Spohr, E.; Schuster, M. Transport in Proton Conductors for Fuel-Cell Applications: Simulations, Elementary Reactions, and Phenomenology. *Chem. Rev.* **2004**, *104*, 4637-4678.

4. Kusoglu, A.; Weber, A. Z. New Insights into Perfluorinated Sulfonic-Acid Ionomers. *Chem. Rev.* **2017**.

5. Allen, F. I.; Comolli, L. R.; Kusoglu, A.; Modestino, M. A.; Minor, A. M.; Weber, A. Z. Morphology of Hydrated as-Cast Nafion Revealed through Cryo Electron Tomography. *ACS Macro Lett.* **2015**, *4*, 1-5.

6. Wang, C.; Clark Ii, J. K.; Kumar, M.; Paddison, S. J. An Ab Initio Study of the Primary Hydration and Proton Transfer of CF3SO3H and CF3O(CF2)2SO3H: Effects of the Hybrid Functional and Inclusion of Diffuse Functions. *Solid State Ionics* **2011**, *199–200*, 6-13.

7. Marcus, Y.; Hefter, G. Ion Pairing. *Chem. Rev.* **2006**, *106*, 4585-4621.

8. Paul, R.; Paddison, S. J. Effects of Dielectric Saturation and Ionic Screening on the Proton Self-Diffusion Coefficients in Perfluorosulfonic Acid Membranes. *J. Chem. Phys.* **2005**, *123*, 224704.

9. Paddison, S. J. Proton Conduction in Pems: Complexity, Cooperativity and Connectivity. In *Device and Materials Modeling in Pem Fuel Cells*, Paddison, S. J., Promislow, K. S., Eds. Springer New York: 2009; pp 385-412.

10. Petersen, M. K.; Voth, G. A. Characterization of the Solvation and Transport of the Hydrated Proton in the Perfluorosulfonic Acid Membrane Nafion. *J. Phys. Chem. B* **2006**, *110*, 18594-18600.

11. Feng, S.; Voth, G. A. Proton Solvation and Transport in Hydrated Nafion. *J. Phys. Chem. B* **2011**, *115*, 5903-5912.

12. Devanathan, R.; Venkatnathan, A.; Dupuis, M. Atomistic Simulation of Nafion Membrane. 2. Dynamics of Water Molecules and Hydronium Ions. *J. Phys. Chem. B* **2007**, *111*, 13006-13013.

13. Gostick, J. T.; Weber, A. Z. Resistor-Network Modeling of Ionic Conduction in Polymer Electrolytes. *Electrochim. Acta* **2015**, *179*, 137-145.

14. Hwang, G. S.; Kaviany, M.; Gostick, J. T.; Kientiz, B.; Weber, A. Z.; Kim, M. H. Role of Water States on Water Uptake and Proton Transport in Nafion Using Molecular Simulations and Bimodal Network. *Polymer* **2011**, *52*, 2584-2593.

15. Spohr, E.; Commer, P.; Kornyshev, A. A. Enhancing Proton Mobility in Polymer Electrolyte Membranes: Lessons from Molecular Dynamics Simulations. *J. Phys. Chem. B* **2002**, *106*, 10560-10569.

16. Bear, J. *Dynamics of Fluids in Porous Media*; Dover: New York, 1988.

17. Eikerling, M.; Kulikovsky, A. A. *Polymer Electrolyte Fuel Cells : Physical Principles of Materials and Operation*; Boca Raton : CRC Press, 2015.

18. Pisani, L.; Valentini, M.; Hofmann, D. H.; Kuleshova, L. N.; D'Aguanno, B. An Analytical Model for the Conductivity of Polymeric Sulfonated Membranes. *Solid State Ionics* **2008**, *179*, 465-476.

19. Choi, P.; Jalani, N. H.; Datta, R. Thermodynamics and Proton Transport in Nafion Ii. Proton Diffusion Mechanisms and Conductivity. *J. Electrochem. Soc.* **2005**, *152*, E123-E130.

20. Eikerling, M.; Kornyshev, A. A.; Stimming, U. Electrophysical Properties of Polymer Electrolyte Membranes: A Random Network Model. *J. Phys. Chem. B* **1997**, *101*, 10807-10820.

21. Eikerling, M.; Kornyshev, A. A.; Kuznetsov, A. M.; Ulstrup, J.; Walbran, S. Mechanisms of Proton Conductance in Polymer Electrolyte Membranes. *J. Phys. Chem. B* **2001**, *105*, 3646-3662.

22. Safiollah, M.; Melchy, P.-E. A.; Berg, P.; Eikerling, M. Model of Water Sorption and Swelling in Polymer Electrolyte Membranes: Diagnostic Applications. *J. Phys. Chem. B* **2015**, *119*, 8165-8175.

23. Berg, P.; Benjaminsen, B. E. Effects of Finite-Size Ions and Relative Permittivity in a Nanopore Model of a Polymer Electrolyte Membrane. *Electrochim. Acta* **2014**, *120*, 429-438.

24. Berrod, Q.; Lyonnard, S.; Guillermo, A.; Ollivier, J.; Frick, B.; Manseri, A.; Améduri, B.; Gébel, G. Nanostructure and Transport Properties of Proton Conducting Self-Assembled Perfluorinated Surfactants: A Bottom-up Approach toward Pfsa Fuel Cell Membranes. *Macromolecules* **2015**, *48*, 6166-6176.

25. Tse, Y.-L. S.; Herring, A. M.; Kim, K.; Voth, G. A. Molecular Dynamics Simulations of Proton Transport in 3m and Nafion Perfluorosulfonic Acid Membranes. *J. Phys. Chem. C* **2013**, *117*, 8079-8091.

26. Savage, J.; Tse, Y.-L. S.; Voth, G. A. Proton Transport Mechanism of Perfluorosulfonic Acid Membranes. *J. Phys. Chem. C* **2014**, *118*, 17436-17445.

27. Clark Ii, J. K.; Paddison, S. J. Ab Initio Molecular Dynamics Simulations of Water and an Excess Proton in Water Confined in Carbon Nanotubes. *Phys. Chem. Chem. Phys.* **2014**, *16*, 17756.

28. Clark Ii, J. K.; Paddison, S. J. Proton Dissociation and Transfer in Proton Exchange Membrane Ionomers with Multiple and Distinct Pendant Acid Groups: An Ab Initio Study. *Electrochim. Acta* **2013**, *101*, 279-292.

29. Devanathan, R.; Idupulapati, N.; Baer, M. D.; Mundy, C. J.; Dupuis, M. Ab Initio Molecular Dynamics Simulation of Proton Hopping in a Model Polymer Membrane. *J. Phys. Chem. B* **2013**, *117*, 16522-16529.

30. Devanathan, R.; Venkatnathan, A.; Dupuis, M. Atomistic Simulation of Nafion Membrane: I. Effect of Hydration on Membrane Nanostructure. *J. Phys. Chem. B* **2007**, *111*, 8069-8079.

31. Choe, Y.-K.; Tsuchida, E.; Ikeshoji, T.; Yamakawa, S.; Hyodo, S.-a. Nature of Proton Dynamics in a Polymer Electrolyte Membrane, Nafion: A First-Principles Molecular Dynamics Study. *Phys. Chem. Chem. Phys.* **2009**, *11*, 3892.

32. Yang, Y.; Pintauro, P. N. Multicomponent Space-Charge Transport Model for Ion-Exchange Membranes with Variable Pore Properties. *Ind. Eng. Chem. Res* **2004**, *43*, 2957-2965.

33. Bontha, J. R.; Pintauro, P. N. Water Orientation and Ion Solvation Effects During Multicomponent Salt Partitioning in a Nafion Cation-Exchange Membrane. *Chem. Eng. Sci.* **1994**, *49*, 3835-3851.

34. Kumar, M.; Edwards, B. J.; Paddison, S. J. A Macroscopic Model of Proton Transport through the Membrane-Ionomer Interface of a Polymer Electrolyte Membrane Fuel Cell. *J. Chem. Phys.* **2013**, *138*, 064903.

35. Paul, R.; Paddison, S. J. Structure and Dielectric Saturation of Water in Hydrated Polymer Electrolyte Membranes: Inclusion of the Internal Field Energy. *J. Phys. Chem. B* **2004**, *108*, 13231-13241.

36. Eikerling, M.; Kornyshev, A. A. Proton Transfer in a Single Pore of a Polymer Electrolyte Membrane. *J. Electroanal. Chem.* **2001**, *502*, 1-14.

37. Commer, P.; Cherstvy, A. G.; Spohr, E.; Kornyshev, A. A. The Effect of Water Content on Proton Transport in Polymer Electrolyte Membranes. *Fuel Cells* **2002**, *2*, 127-136.

38. Kusoglu, A.; Shi, S.; Weber, A. Z. in preperation.

39. Shi, S.; Weber, A. Z.; Kusoglu, A. Structure-Transport Relationship of Perfluorosulfonic-Acid Membranes in Different Cationic Forms. *Electrochim. Acta* **2016**, *220*, 517-528.

40. Kreuer, K.-D.; Portale, G. A Critical Revision of the Nano-Morphology of Proton Conducting Ionomers and Polyelectrolytes for Fuel Cell Applications. *Adv. Funct. Mater.* **2013**, *23*, 5390-5397.

41. Crothers, A. R.; Radke, C. J.; Weber, A. Z. Multiscale Model of Proton Transport in Perfluorosulfonic-Acid Membrane. *ECS Transactions* **2015**, *69*, 731-742.

42. Newman, J.; Thomas-Alyea, K. E. *Electrochemical Systems*; John Wiley & Sons, 2004, p 674.

43. Hirschfelder, J. O.; Curtiss, C. F.; Bird, R. B.; Mayer, M. G. *Molecular Theory of Gases and Liquids*; Wiley New York, 1954; Vol. 26.

44. Bird, R. B.; Lightfoot, E. N.; Stewart, E. W. *Transport Phenomenon*; Wiley, 2007.

45. Brenner, H. The Slow Motion of a Sphere through a Viscous Fluid Towards a Plane Surface. *Chem. Eng. Sci.* **1961**, *16*, 242-251.

46. Goldman, A. J.; Cox, R. G.; Brenner, H. Slow Viscous Motion of a Sphere Parallel to a Plane Wall—I Motion through a Quiescent Fluid. *Chem. Eng. Sci.* **1967**, *22*, 637-651.

47. Faxén, H. Der Widerstand Gegen Die Bewegung Einer Starren Kugel in Einer Zähen Flüssigkeit, Die Zwischen Zwei Parallelen Ebenen Wänden Eingeschlossen Ist. *Annalen der Physik* **1922**, *373*, 89-119.

48. Hubbard, J. B. Dielectric Dispersion and Dielectric Friction in Electrolyte Solutions. II. *J. Chem. Phys.* **1978**, *68*, 1649-1664.

49. Zoski, C. G. *Handbook of Electrochemistry*; Elsevier, 2006, p 935.

50. Bontha, J. R.; Pintauro, P. N. Prediction of Ion Solvation Free Energies in a Polarizable Dielectric Continuum. *J. Phys. Chem.* **1992**, *96*, 7778-7782.

51. Marcus, Y. Ions and Their Properties. In *Ions in Solution and Their Solvation*, John Wiley & Sons, Inc: 2015; pp 10-62.

52. Bockris, J. O. M.; Conway, B. E.; White, R. E. *Modern Aspects of Electrochemistry*; Springer Science & Business Media, 2012; Vol. 22.

53. Noyes, R. M. Thermodynamics of Ion Hydration as a Measure of Effective Dielectric Properties of Water. *J. Am. Chem. Soc.* **1962**, *84*, 513-522.

54. Palascak, M. W.; Shields, G. C. Accurate Experimental Values for the Free Energies of Hydration of H+, Oh-, and H3o+. *J. Phys. Chem. A* **2004**, *108*, 3692-3694.

55. Robinson, R. A.; Stokes, R. H. *Electrolyte Solutions*; Courier Corporation, 2002.

56. *CRC Handbook of Chemistry and Physics*; Cleveland, Ohio : CRC Press, 1978.

57. Vacha, R.; Buch, V.; Milet, A.; Devlin, J. P.; Jungwirth, P. Autoionization at the Surface of Neat Water: Is the Top Layer Ph Neutral, Basic, or Acidic? *Phys. Chem. Chem. Phys.* **2007**, *9*, 4736-4747.

58. Bikerman, J. XXXIX. Structure and Capacity of Electrical Double Layer. *Philos. Mag. (1798-1977)* **1942**, *33*, 384-397.

59. Bazant, M. Z.; Kilic, M. S.; Storey, B. D.; Ajdari, A. Towards an Understanding of Induced-Charge Electrokinetics at Large Applied Voltages in Concentrated Solutions. *Adv. Colloid Interface Sci.* **2009**, *152*, 48-88.

60. Ehrlich, P. Dielectric Properties of Teflon from Room Temperature to 314 C and from Frequencies of 102 to 105 C/S. *J. Res. Nat. Bur. Stand* **1953**, *51*, 185-8.

61. Karraker, K. A.; Radke, C. J. Disjoining Pressures, Zeta Potentials and Surface Tensions of Aqueous Non-Ionic Surfactant/Electrolyte Solutions: Theory and Comparison to Experiment. *Adv. Colloid Interface Sci.* **2002**, *96*, 231-264.

62. Onsager, L.; Samaras, N. N. T. The Surface Tension of Debye-Hückel Electrolytes. *J. Chem. Phys.* **1934**, *2*, 528-536.

63. Booth, F. The Dielectric Constant of Water and the Saturation Effect. *J. Chem. Phys.* **1951**, *19*, 391-394.

64. Lamm, G.; Pack, G. R. Calculation of Dielectric Constants near Polyelectrolytes in Solution. *J. Phys. Chem. B* **1997**, *101*, 959-965.

65. Gur, Y.; Ravina, I.; Babchin, A. J. On the Electrical Double Layer Theory. Ii. The Poisson—Boltzmann Equation Including Hydration Forces. *J. Colloid Interface Sci.* **1978**, *64*, 333-341.

66. Haggis, G. H.; Hasted, J. B.; Buchanan, T. J. The Dielectric Properties of Water in Solutions. *J. Chem. Phys.* **1952**, *20*, 1452-1465.

67. Yang, Y.; Pintauro, P. N. Multicomponent Space-Charge Transport Model for Ion-Exchange Membranes. *AIChE J.* **2000**, *46*, 1177-1190.

68. Chang, Y.; Mohanty, A. D.; Smedley, S. B.; Abu-Hakmeh, K.; Lee, Y. H.; Morgan, J. E.; Hickner, M. A.; Jang, S. S.; Ryu, C. Y.; Bae, C. Effect of Superacidic Side Chain Structures on High Conductivity Aromatic Polymer Fuel Cell Membranes. *Macromolecules* **2015**, *48*, 7117-7126.

69. Hristov, I. H.; Paddison, S. J.; Paul, R. Molecular Modeling of Proton Transport in the Short-Side-Chain Perfluorosulfonic Acid Ionomer. *J. Phys. Chem. B* **2008**, *112*, 2937-2949.

70. Currie, J. A. Gaseous Diffusion in Porous Media. Part 2. - Dry Granular Materials. *Br. J. Appl. Phys.* **1960**, *11*, 318.

71. Takamatsu, T.; Eisenberg, A. Densities and Expansion Coefficients of Nafion Polymers. *J. Appl. Polym. Sci.* **1979**, *24*, 2221-2235.

72. Yasuda, H.; Lamaze, C. E.; Peterlin, A. Diffusive and Hydraulic Permeabilities of Water in Water-Swollen Polymer Membranes. *J. Polym. Sci. A-2 Polym. Phys.* **1971**, *9*, 1117-1131.

73. Giffin, G. A.; Haugen, G. M.; Hamrock, S. J.; Di Noto, V. Interplay between Structure and Relaxations in Perfluorosulfonic Acid Proton Conducting Membranes. *J. Am. Chem. Soc.* **2013**, *135*, 822-834.

74. Roy, A.; Hickner, M. A.; Yu, X.; Li, Y.; Glass, T. E.; McGrath, J. E. Influence of Chemical Composition and Sequence Length on the Transport Properties of Proton Exchange Membranes. *J. Polym. Sci., Part B: Polym. Phys.* **2006**, *44*, 2226-2239.

75. Bae, B.; Yoda, T.; Miyatake, K.; Uchida, H.; Watanabe, M. Proton-Conductive Aromatic Ionomers Containing Highly Sulfonated Blocks for High-Temperature-Operable Fuel Cells. *Angew. Chem. Int. Ed.* **2010**, *49*, 317-320.

76. Evans, D. F.; Tominaga, T.; Hubbard, J. B.; Wolynes, P. G. Ionic Mobility. Theory Meets Experiment. *J. Phys. Chem.* **1979**, *83*, 2669-2677.

77. Collazo, N.; Shin, S.; Rice, S. A. Molecular-Dynamics Studies of the Structure and Properties of Monolayers of Perfluorinated Amphiphiles. *J. Chem. Phys.* **1992**, *96*, 4735-4742.

TOC Graphic